

Shear stress sensing with Bragg grating-based sensors in microstructured optical fibers

Sanne Sulejmani,^{1,*} Camille Sonnenfeld,¹ Thomas Geernaert,¹ Geert Luyckx,² Danny Van Hemelrijck,³ Pawel Mergo,⁴ Waclaw Urbanczyk,⁵ Karima Chah,⁶ Christophe Caucheteur,⁶ Patrice Mégret,⁶ Hugo Thienpont¹ and Francis Berghmans¹

¹Brussels Photonics Team (B-PHOT), Vrije Universiteit Brussel, Pleinlaan 2, 1050 Brussel, Belgium

²Department of Materials Science and Engineering, Universiteit Gent, Technologiepark 903, 9052 Gent, Belgium

³Department of Mechanics of Materials and Constructions, Vrije Universiteit Brussel, Pleinlaan 2, 1050 Brussel, Belgium

⁴Department of Optical Fiber Technology, Marie Curie-Skłodowska University, Pl. M. Curie-Skłodowskiej 3, 20-031 Lublin, Poland

⁵Institute of Physics, Wrocław University of Technology, Wybrzeże Wyspińskiego 27, 50-370 Wrocław, Poland

⁶Electromagnetism and Telecom Department, University of Mons, Mons 7000, Belgium

*ssulejma@b-phot.org

Abstract: We demonstrate shear stress sensing with a Bragg grating-based microstructured optical fiber sensor embedded in a single lap adhesive joint. We achieved an unprecedented shear stress sensitivity of 59.8 pm/MPa when the joint is loaded in tension. This corresponds to a shear strain sensitivity of 0.01 pm/ $\mu\epsilon$. We verified these results with 2D and 3D finite element modeling. A comparative FEM study with conventional highly birefringent side-hole and bow-tie fibers shows that our dedicated fiber design yields a fourfold sensitivity improvement.

©2013 Optical Society of America

OCIS codes: (060.2370) Fiber optics sensors; (120.3940) Metrology.

References and links

1. A. Cusano, A. Cutolo, and J. Albert, *Fiber Bragg Grating Sensors: Recent Advancements, Industrial Applications and Market Exploitation* (Bentham Science Publishers, 2011).
2. F. Berghmans and T. Geernaert, "Optical fiber point sensors" in *Advanced Fiber Optics: Concepts and Technology*, L. Thévenaz, Ed. (EPFL Press, 2011) pp. 308–344.
3. A. Othonos and K. Kalli, *Fiber Bragg gratings: Fundamentals and applications in telecommunications and sensing* (Artech House, 1999).
4. G. Luyckx, E. Voet, N. Lammens, and J. Degrieck, "Strain measurements of composite laminates with embedded fibre bragg gratings: criticism and opportunities for research," *Sensors (Basel)* **11**(1), 384–408 (2011).
5. C. Martelli, J. Canning, N. Groothoff, and K. Lyytikäinen, "Strain and temperature characterization of photonic crystal fiber Bragg gratings," *Opt. Lett.* **30**(14), 1785–1787 (2005).
6. T. Mawatari and D. Nelson, "A multi-parameter Bragg grating fiber optic sensor and triaxial strain measurement," *Smart Mater. Struct.* **17**(3), 035033 (2008).
7. C. Jewart, K. P. Chen, B. McMillen, M. M. Bails, S. P. Levitan, J. Canning, and I. V. Avdeev, "Sensitivity enhancement of fiber Bragg gratings to transverse stress by using microstructural fibers," *Opt. Lett.* **31**(15), 2260–2262 (2006).
8. T. Geernaert, G. Luyckx, E. Voet, T. Nasilowski, K. Chah, M. Becker, H. Bartelt, W. Urbanczyk, J. Wojcik, W. De Waele, J. Dearieck, H. Terryn, F. Berghmans, and H. Thienpont, "Transversal load sensing with fiber Bragg gratings in microstructured optical fibers," *IEEE Photon. Technol. Lett.* **21**(1), 6–8 (2009).
9. E. Chmielewska, W. Urbańczyk, and W. J. Bock, "Measurement of pressure and temperature sensitivities of a Bragg grating imprinted in a highly birefringent side-hole fiber," *Appl. Opt.* **42**(31), 6284–6291 (2003).
10. H.-M. Kim, T.-H. Kim, B. Kim, and Y. Chung, "Enhanced transverse load sensitivity by using a highly birefringent photonic crystal fiber with larger air holes on one axis," *Appl. Opt.* **49**(20), 3841–3845 (2010).
11. www.tekscan.com
12. www.hbm.com/en/menu/products/strain-gages-accessories/
13. R. Khandan, S. Noroozi, P. Sewell, and J. Vinney, "The development of laminated composite plate theories: a review," *J. Mater. Sci.* **47**(16), 5901–5910 (2012).
14. K. Basler, *Strength of Plate Girders in Shear* (Lehigh University Institute of Research, 1960).
15. E. Real, E. Mirambell, and I. Estrada, "Shear response of stainless steel plate girders," *Eng. Struct.* **29**(7), 1626–1640 (2007).

16. M. D. Banea and L. F. M. da Silva, "Adhesively bonded joints in composite materials: An overview," *Proc. Inst. Mech. Eng. L J*, Mater. Des. Appl. **223**, 1–18 (2009).
17. S. Benyoucef, A. Tounsi, E. A. Adda Bedia, and S. A. Meftah, "Creep and shrinkage effect on adhesive stresses in RC beams strengthened with composite laminates," *Compos. Sci. Technol.* **67**(6), 933–942 (2007).
18. H. Yousef, M. Boukallel, and K. Althoefer, "Tactile sensing for dexterous in-hand manipulation in robotics—A review," *Sens., Actuator A-Phys* **167**(2), 171–187 (2011).
19. M. I. Tiwana, S. J. Redmond, and N. H. Lovell, "A review of tactile sensing technologies with applications in biomedical engineering," *Sens., Actuator A-Phys* **179**, 17–31 (2012).
20. C. Perry, "Plane-shear measurement with strain gages," *Exp. Mech.* **9**(19–N), 22 (1969).
21. J. W. Naughton and M. Sheplak, "Modern developments in shear-stress measurement," *Prog. Aerosp. Sci.* **38**(6–7), 515–570 (2002).
22. K. Noda, K. Hoshino, K. Matsumoto, and I. Shimoyama, "A shear stress sensor for tactile sensing with the piezoresistive cantilever standing in elastic material," *Sens., Actuator A-Phys* **127**(2), 295–301 (2006).
23. H.-K. Lee, J. Chung, S.-I. Chang, and E. Yoon, "Normal and shear force measurement using a flexible polymer tactile sensor with embedded multiple capacitors," *J. Microelectromech. Syst.* **17**(4), 934–942 (2008).
24. K. Sundara-Rajan, A. Bestick, G. I. Rowe, G. K. Klute, W. R. Ledoux, H. C. Wang, and A. V. Mamishev, "An interfacial stress sensor for biomechanical applications," *Meas. Sci. Technol.* **23**(8), 085701 (2012).
25. J. Missinne, E. Bosman, B. Van Hoe, G. Van Steenberge, S. Kalathimekkad, P. Van Daele, and J. Vanfleteren, "Flexible shear sensor based on embedded optoelectronic components," *IEEE Photon. Technol. Lett.* **23**(12), 771–773 (2011).
26. W.-C. Wang, W. R. Ledoux, B. J. Sangeorzan, and P. G. Reinhall, "A shear and plantar pressure sensor based on fiber-optic bend loss," *J. Rehabil. Res. Dev.* **42**(3), 315–325 (2005).
27. S. C. Tjin, R. Suresh, and N. Q. Ngo, "Fiber Bragg grating based shear-force sensor: modeling and testing," *J. Lightwave Technol.* **22**(7), 1728–1733 (2004).
28. A. Candiani, W. Margulis, M. Konstantaki, and S. Pissadakis, "Ferrofluid-infiltrated optical fibers for shear-sensing smart pads," *SPIE Newsroom* (2012).
29. W. L. Schulz, E. Udd, M. Morrell, J. M. Seim, I. M. Perez, and A. Trego, "Health monitoring of an adhesive joint using a multi-axis fiber grating strain sensor system," in *Proc. SPIE 3586*, "Nondestructive Evaluation of Aging Aircraft, Airports, and Aerospace Hardware **III**", 41–52 (1999).
30. J. C. Knight, "Photonic crystal fibres," *Nature* **424**(6950), 847–851 (2003).
31. P. S. J. Russell, "Photonic-crystal fibers," *J. Lightwave Technol.* **24**(12), 4729–4749 (2006).
32. W. Urbanczyk, T. Martynkien, M. Szpulak, G. Statkiewicz, J. Olszewski, G. Gojuch, J. Wojcik, P. Mergo, M. Makara, T. Nasilowski, F. Berghmans, and H. Thienpont, in *Proc. SPIE 6619*, Third European Workshop on Optical Fibre Sensors, "Photonic crystal fibers: new opportunities for sensing," 66190G–66190G (2007).
33. O. Frazão, J. Santos, F. Araújo, and L. Ferreira, "Optical sensing with photonic crystal fibers," *Laser Photon. Rev.* **2**(6), 449–459 (2008).
34. T. Martynkien, G. Statkiewicz-Barabach, J. Olszewski, J. Wojcik, P. Mergo, T. Geernaert, C. Sonnenfeld, A. Anuszkiewicz, M. K. Szczurowski, K. Tarnowski, M. Makara, K. Skorupski, J. Klimek, K. Poturaj, W. Urbanczyk, T. Nasilowski, F. Berghmans, and H. Thienpont, "Highly birefringent microstructured fibers with enhanced sensitivity to hydrostatic pressure," *Opt. Express* **18**(14), 15113–15121 (2010).
35. S. Sulejmani, C. Sonnenfeld, T. Geernaert, P. Mergo, M. Makara, K. Poturaj, K. Skorupski, T. Martynkien, G. Statkiewicz-Barabach, J. Olszewski, W. Urbanczyk, C. Caucheteur, K. Chah, P. Mégret, H. Terryn, J. Van Roosbroeck, F. Berghmans, and H. Thienpont, "Control over the pressure sensitivity of Bragg-grating based sensors in highly birefringent microstructured optical fibers," *IEEE Photon. Technol. Lett.* **24**(6), 527–529 (2012).
36. T. Geernaert, T. Nasilowski, K. Chah, M. Szpulak, J. Olszewski, G. Statkiewicz, J. Wojcik, K. Poturaj, W. Urbanczyk, M. Becker, M. Rothhardt, H. Bartelt, F. Berghmans, and H. Thienpont, "Fiber Bragg gratings in Germanium-doped highly birefringent microstructured optical fibers," *IEEE Photon. Technol. Lett.* **20**(8), 554–556 (2008).
37. T. Geernaert, M. Becker, P. Mergo, T. Nasilowski, J. Wojcik, W. Urbanczyk, M. Rothhardt, C. Chojetzki, H. Bartelt, H. Terryn, F. Berghmans, and H. Thienpont, "Bragg grating inscription in GeO₂-doped microstructured optical fibers," *J. Lightwave Technol.* **28**(10), 1459–1467 (2010).
38. F. Berghmans, T. Geernaert, T. Baghdasaryan, and H. Thienpont, "Challenges in the fabrication of fibre Bragg gratings in silica and polymer microstructured optical fibres," *Laser Photon. Rev.* 10.1002/lpor.201200103 (2013).
39. C. Sonnenfeld, S. Sulejmani, T. Geernaert, S. Eve, N. Lammens, G. Luyckx, E. Voet, J. Degrieck, W. Urbanczyk, P. Mergo, M. Becker, H. Bartelt, F. Berghmans, and H. Thienpont, "Microstructured optical fiber sensors embedded in a laminate composite for smart material applications," *Sensors (Basel)* **11**(12), 2566–2579 (2011).
40. F. Berghmans, T. Geernaert, S. Sulejmani, H. Thienpont, G. Van Steenberge, B. Van Hoe, P. Dubruel, W. Urbanczyk, P. Mergo, D. J. Webb, K. Kalli, J. Van Roosbroeck, and K. Sugden, "Photonic crystal fiber Bragg grating based sensors: opportunities for applications in healthcare," in *Communications and Photonics Conference and Exhibition, 2011. ACP*, Asia **8311**, 1–10 (2011).
41. G. Luyckx, E. Voet, T. Geernaert, K. Chah, T. Nasilowski, W. De Waele, W. Van Paeppegem, M. Becker, H. Bartelt, W. Urbanczyk, J. Wojcik, J. Degrieck, F. Berghmans, and H. Thienpont, "Response of FBGs in

- microstructured and bow tie fibers embedded in laminated composite,” *IEEE Photon. Technol. Lett.* **21**(18), 1290–1292 (2009).
42. L. F. M. da Silva, P. J. C. das Neves, R. D. Adams, A. Wang, and J. K. Spelt, “Analytical models of adhesively bonded joints—Part II: Comparative study,” *Int. J. Adhes. Adhes.* **29**(3), 331–341 (2009).
 43. M. Goland and E. Reissner, *J. Appl. Mech. Trans. Am. Soc. Eng.* **66**, A17 (1944).
 44. C. M. Lawrence, D. V. Nelson, and E. Udd, “Multiparameter sensing with fiber Bragg gratings,” in *Pacific Northwest Fiber Optic Sensor Workshop* **2872** (1996), 24–31.
 45. C. M. Lawrence, D. V. Nelson, E. Udd, and T. Bennett, “A fiber optic sensor for transverse strain measurement,” *Exp. Mech.* **39**(3), 202–209 (1999).
 46. F. Berghmans, T. Geernaert, M. Napierala, T. Baghdasaryan, C. Sonnenfeld, S. Sulejmani, T. Nasilowski, P. Mergo, T. Martynkien, W. Urbańczyk, E. Beres-Pawlik, and H. Thienpont, “Applying optical design methods to the development of application specific photonic crystal fibres,” in *Proc. SPIE* **8550**, Optical Systems Design (2012), 85500B.
 47. S. Sulejmani, C. Sonnenfeld, T. Geernaert, F. Berghmans, H. Thienpont, S. Eve, N. Lammens, G. Luyckx, E. Voet, J. Degrieck, W. Urbanczyk, P. Mergo, M. Becker, and H. Bartelt, “Towards micro-structured optical fiber sensors for transverse strain sensing in smart composite materials,” in *2011 IEEE Sensors* (2011), pp. 109–112.
 48. K. Chah, D. Kinet, M. Wuilpart, P. Mégret, and C. Caucheteur, “Femtosecond-laser-induced highly birefringent Bragg gratings in standard optical fiber,” *Opt. Lett.* **38**(4), 594–596 (2013).
 49. www.3ds.com/products/simulia/portfolio/abaqus/
 50. E. Chehura, C.-C. Ye, S. E. Staines, S. W. James, and R. P. Tatam, “Characterization of the response of fibre Bragg gratings fabricated in stress and geometrically induced high birefringence fibres to temperature and transverse load,” *Smart Mater. Struct.* **13**(4), 888–895 (2004).
 51. www.instron.com
 52. www.fbgs.com
 53. Pliogrip 1000/1040/1060/1080 Acrylic Adhesive System (Ashland Performance Materials) – Technical datasheet.
 54. DP-8005 (3M Scotch Weld) – Technical Datasheet.
 55. A. M. G. Pinto, A. G. Magalhães, R. D. S. G. Campilho, M. F. S. F. de Moura, and A. P. M. Baptista, “Single-lap joints of similar and dissimilar adherends bonded with an Acrylic adhesive,” *J. Adhes.* **85**(6), 351–376 (2009).
 56. M. S. Muller, T. C. Buck, H. J. El-Khozondar, and A. W. Koch, “Shear strain influence on fiber Bragg grating measurement systems,” *J. Lightwave Technol.* **27**(23), 5223–5229 (2009).
 57. W. Urbanczyk, E. Chmielewska, and W. J. Bock, “Measurements of temperature and strain sensitivities of a two-mode Bragg grating imprinted in a bow-tie fibre,” *Meas. Sci. Technol.* **12**(7), 800–804 (2001).
 58. R. Guan, F. Zhu, Z. Gan, D. Huang, and S. Liu, “Stress birefringence analysis of polarization maintaining optical fibers,” *Opt. Fiber Technol.* **11**(3), 240–254 (2005).
 59. J. R. Clowes, S. Syngellakis, and M. N. Zervas, “Pressure sensitivity of side-hole optical fiber sensors,” *IEEE Photon. Technol. Lett.* **10**(6), 857–859 (1998).
-

1. Introduction

The wide adoption of smart materials and structural health monitoring in domains such as material manufacturing, civil engineering, transport, energy production and healthcare stimulates the demand for reliable and dedicated sensors. Typical physical quantities to measure include temperature, pressure or strain. Conventional electromechanical sensors, such as electrical strain gauges, are often perfectly adequate for this task. However, an increasing number of smart sensor applications require the sensor to be read out permanently whilst being embedded in a non-invasive manner in various materials that are often subjected to harsh conditions over long lifetimes. Electromechanical sensors are not always suited for this challenge, as they are usually bulky, they exhibit intrinsic temperature sensitivity, they are vulnerable to electromagnetic interference and they can exhibit a strong signal drift. When traditional sensors fail, optical fiber sensors and more specifically fiber Bragg grating (FBG) sensors, can provide a solution. FBG sensors feature many advantages over conventional sensors; they are small, flexible and lightweight, they can be multiplexed and allow quasi-distributed sensor configurations, they allow absolute measurements and they have a linear response over a wide temperature and mechanical strain range. These features make FBG sensors highly suitable for integration in a material for smart sensing applications [1–4].

Multi-axial (selective) strain sensing remains a challenge for structural health monitoring or tactile sensing applications. Many research efforts focused on axial strain, hydrostatic pressure and transverse strain sensors and there are currently various methods commercially available with a high strain sensing resolution [5–12]. On the contrary, the detection of shear strain remained mostly unaddressed, and at present no adequate sensor exists that is

intrinsically sensitive to shear deformation. Shear stress nevertheless plays a crucial role in the appearance of structural defects such as delamination in laminated composite materials, debonding of adhesive joints or buckling of beams [13–17]. In addition, shear stress sensing is also a key feature of tactile sensors, since this parameter provides information on (skin) friction [18,19]. The absence of shear sensing technology can be attributed to the challenging requirements for a shear stress sensor. Non-intrusive integration capabilities and flexibility are essential features of a shear sensor. Furthermore, high shear sensing resolution is indispensable since shear stress levels in aforementioned structures and applications are typically several orders of magnitude smaller than normal stress. Depending on the specific sensor implementation, different types of shear force sensors have been investigated. A plane-shear strain gage rosette was first demonstrated in [20]. Current developments of shear stress sensors are based on MEMS technology [21], including piezo-resistive [22] or capacitive [23,24] shear stress sensors. More recently, Missine *et al.* [25] demonstrated an optoelectronic shear sensor based on measuring the optical power with a photodiode received from a vertical cavity surface-emitting laser facing the photodiode and separated with a deformable transduction layer. Distributed shear force sensing was also proposed by Wang *et al.* [26] using an array of optical fibers embedded in a flexible polymer foil. Shear or transverse loading of the foil induces macro bending of the fibers which can be observed through intensity attenuations.

Research on shear strain sensors using FBG sensors has so far focused on 3 very different approaches. A first technique, demonstrated by Tjin *et al.* [27], uses a FBG in a conventional single mode fiber (SMF) that is embedded under a small tilt angle in a deformable layer. Shear loading of this layer induces an axial strain to the fiber, which can be derived from the Bragg peak wavelength shift. Candiani *et al.* [28] has demonstrated a shear sensing pad by embedding a ferrofluidic-infiltrated microstructured optical fiber FBG sensor and a magnet in a polymer foil. When a shear load is applied to the foil, the location of the ferrofluidic segment in the FBG sensor changes, which in its turn influences the FBG reflection spectrum. Another approach, reported by Schulz *et al.* [29], uses a conventional highly birefringent FBG sensor that is embedded in a material perpendicular to the direction of an applied shear load. When the fundamental optical axes of the fiber are aligned with the directions of principal stress, the optical fiber experiences the shear load as if it were a transverse load. In this manner, the applied shear load induces a change in material birefringence of the optical fiber, and hence also a change in its modal birefringence. This can be detected by monitoring the FBG reflection spectrum.

The FBG sensors used in the work of Schulz *et al.* [29], for example, typically featured low shear strain sensitivity and significant thermal cross-sensitivity. In order to deal with these issues we propose to work with highly birefringent microstructured optical fibers (MOF). Owing to the unique features of MOFs, leveraged by the properties of FBG sensors, they have become a promising technology for optical fiber based sensing [30–33]. While the cross section of a conventional step-index optical fiber is entirely made of (silica) glass, the cross section of a MOF displays a pattern of air holes that run along the entire length of the fiber. The arrangement of these holes determines the optomechanical properties of the MOF. By changing the geometry, position, shape or number of holes, fiber properties such as optical mode confinement, modal dispersion, modal birefringence and thermal sensitivity can be tuned. By exploiting stress induced changes of the modal birefringence of a highly birefringent MOF, temperature insensitive pressure and transverse strain FBG sensors have been demonstrated [34,35]. When a mechanical load is applied to the cladding of such a MOF, the asymmetric air hole geometry will induce an asymmetric stress distribution in the core region, which affects the material birefringence, and hence also the modal birefringence. Temperature insensitivity can be attained by using only low GeO₂-doping levels in the core region to limit thermal stress variations. A small concentration of GeO₂ is still required to allow for FBG inscription using conventional UV techniques [36–38].

Our previous research resulted in a dedicated MOF-FBG sensor ('butterfly MOF') with unprecedented transverse strain sensitivity, combined with a very low thermal sensitivity [34,39]. Here we show that the record transverse strain sensitivity of the butterfly MOF-FBG sensor is translated in an unprecedented shear strain sensitivity, exceeding that achieved with conventional highly birefringent fibers with a factor 4 (section 3). By aligning the transverse strain sensing axes of the butterfly MOF with the directions of principal stress in a shear loaded material, we can detect shear strain. In this work, we successfully demonstrate shear strain sensing by embedding the butterfly MOF-FBG in the adhesive layer of a single lap adhesive joint (SLJ). We chose to embed our sensor in a lap joint structure because the shear stress distribution in the adhesive layer is well known and can be described by analytical models (section 2). One application of the shear stress sensor is to assess the shear stress distribution in complex prototype joints. Since the shear stress distribution in an adhesive bond line can be a measure of the bond quality, the sensor could in principle also be used for monitoring adhesive bonds in large structures. However, since our sensor is intrinsically sensitive to shear stress, it can as well be implemented in other materials or structures, such as polymer [40] or composite materials [39,41].

Our paper is structured as follows. In section 2 we discuss how a highly birefringent MOF-FBG sensor can detect shear stress in a single lap adhesive joint (SLJ). In section 3 we elaborate on the experimental results that we have obtained when using butterfly MOF-FBG sensors to measure shear stress in an SLJ experiment. We also verify our experimental results with 2D and 3D finite element modeling techniques. Finally, in section 4, we conclude on the shear stress sensing opportunities offered by our dedicated selective strain sensors.

2. Shear stress sensing with highly birefringent optical fiber sensors

To determine the shear stress sensing performance of a butterfly MOF-FBG sensor (Fig. 1), we have embedded several of these sensors in a single lap adhesive joint (SLJ). A SLJ is a simple structure for which the shear stress distribution in the adhesive layer is well known and can be described by analytical models [42]. The analysis of Goland-Reissner [43] is a classic two-dimensional linear elastic method to analyze SLJs and to determine not only the shear stress in the bond layer, but also the peel stress that is induced by the bending moment caused by eccentric loading of the joint. Figure 2(a) shows a SLJ configuration with additional spacer tabs placed at the ends of the adherends to ensure tensile loading along the center line $y = 0$. Figure 2(b) compares the shear and peel stress profile from Goland-Reissner theory, and that from 2D finite element modeling (see section 3) of the SLJ shown in Fig. 2(a). This profile demonstrates that in the centre of the adhesive layer – at the location of the optical fiber - shear stress is more prominent than peel stress. However, at the edges of the overlap, peel stress will dominate. This peel stress may also initiate joint failure. It is worthwhile mentioning that the Goland-Reissner analysis does not include the decay of shear and peel stress near the edges of the adhesive bond. The nearly linear evolution of the shear and peel stress, with correlation coefficients $R^2 > 0.999$ and $R^2 > 0.998$, respectively, in the centre of the adhesive layer when the tensile loading is increased is shown in Fig. 2(c).

The operating principle of the butterfly MOF-FBG sensor relies on the change of modal birefringence caused by mechanical load applied to the cladding of the MOF, or to the material in which the sensor is embedded. Because of the asymmetric geometry of the air hole pattern, load applied to the fiber induces an asymmetric mechanical stress distribution in the core region. The refractive indices for the modes polarized along the x - and y -direction, n_x and n_y , are therefore affected in a different manner according to [44–46]:

$$n_i = n(x, y) + \Delta n_i(x, y) \quad (1)$$

with $i = x$ or y for the x - or y -polarized modes. The correction terms $\Delta n_i(x, y)$ represent the change in stress distribution induced by mechanical load:

$$\Delta n_x(x, y) = C_1 \sigma_1(x, y) + C_2 [\sigma_2(x, y) + \sigma_3(x, y)] \quad (2)$$

$$\Delta n_y(x, y) = C_1 \sigma_2(x, y) + C_2 [\sigma_1(x, y) + \sigma_3(x, y)] \quad (3)$$

with C_1 and C_2 the stress-optic coefficients. The principal stresses $\sigma_1(x, y)$ and $\sigma_2(x, y)$ are determined from the normal stress components $\sigma_x(x, y)$ and $\sigma_y(x, y)$ and shear stress component $\tau_{xy}(x, y)$ using the following relationship:

$$\sigma_{1,2} = \frac{(\sigma_x + \sigma_y) \pm \sqrt{(\sigma_x - \sigma_y)^2 + 4\tau_{xy}^2}}{2} \quad (4)$$

The influence of the shear stress component is often neglected when transverse stress sensitivity of a MOF-FBG sensor is being considered. However, when investigating the shear stress sensitivity of these sensors, the contribution of this component is of major importance.

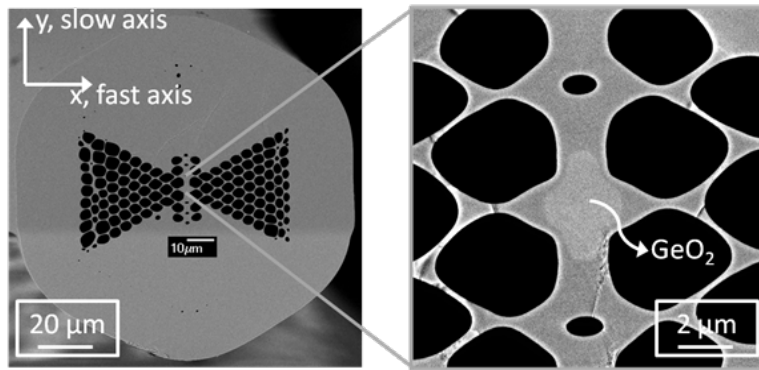


Fig. 1. The butterfly MOF-FBG sensor has an asymmetric air hole topology which induces large deformations in the core region and its GeO_2 doped inclusion during fiber fabrication [34]. The contours of the air holes, doped region and cladding are reconstructed in a 2D geometry for FEM simulations in Abaqus.

Because of the large asymmetry in the design of the butterfly MOF, the sensitivity of the sensor to transverse load depends on the angular orientation of the MOF with respect to the direction of the load. More specifically, the butterfly MOF-FBG sensor has a sine-like angular dependence of the transverse line load [39] and transverse strain sensitivity when embedded in a material [47]. The transverse strain sensitivity is highest when the transverse load is applied along 90° , which is indicated in Fig. 1 by the y -axis and which is also called ‘slow axis’. When the fiber is loaded along 0° , which corresponds to the x -axis, or so-called ‘fast axis’, the magnitude of the sensitivity is still large, but it will now be negative. When the fiber is transversally loaded along $\pm 45^\circ$, the magnitude of its transverse line loading sensitivity approaches zero. When embedded in a shear loaded adhesive layer along $\pm 45^\circ$ (Fig. 2(a).), it will detect the shear load induced transverse strain in the fiber. At the same time, the influence of peel strain on the sensor signal will remain low.

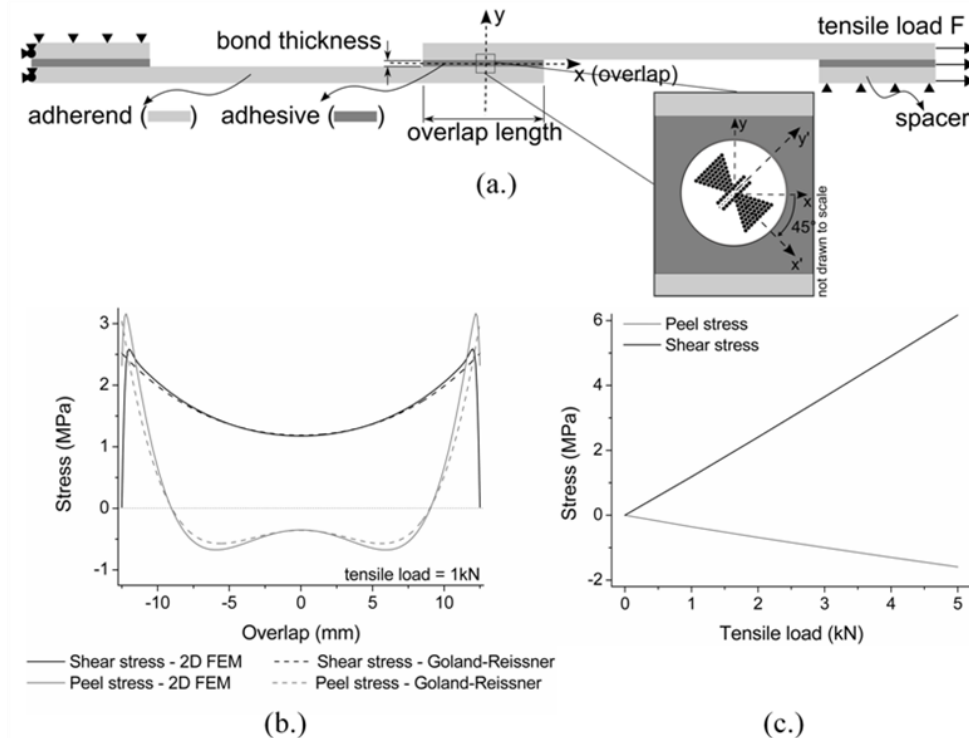


Fig. 2. (a) Configuration of the tested and modeled SLJ with an optical fiber embedded in the centre ($x = y = 0$) of the adhesive layer. The boundary and loading conditions used for 2D and 3D FEM analyses are indicated. Perfect bonding is assumed at every interface. (b) Shear and peel stress profile along the adhesive bond line ($y = 0$) in a SLJ according to Goland-Reissner analysis and obtained with 2D FEM modeling of a SLJ configuration as shown in (a). The addition of spacer tabs (which is not considered in the Goland-Reissner model) has a small influence on the stress profile near the edges of the adhesive overlap. (c) The evolution of the shear and peel stress in the centre of the adhesive layer due to tensile loading is nearly linear ($R^2 > 0.999$ and $R^2 > 0.998$, respectively).

3. Experimental and FEM modeling results

We carry out experiments on FBG sensors embedded in SLJs that are loaded in tension up to failure and 2D and 3D structural finite element (FEM) analyses of an optical fiber embedded in a SLJ to compute and verify the sensor response. We embed two FBG sensors fabricated in a conventional SMF (referred to as sample 1A and 1B) and two sensors fabricated in a butterfly MOF (sample 2A and 2B) in a SLJ. The joint configuration is shown in Fig. 2(a) with the optical fiber located in the centre of the adhesive layer and directed along the z -direction. The adhesive is a two component methyl methacrylate (Simson Supergrip MMA 8105) that has cured at room temperature for at least 24h. The length and thickness of the adhesive layer are indicated in Table 1 for each sample. Schulz *et al.* [29] have demonstrated before that the presence of an optical fiber in an adhesive bond layer does not affect its strength. The adherends are made of aluminum. To ensure that tensile loading is along the central axis ($y = 0$) of the SLJ, spacer tabs are placed at the ends of the adherends where they are gripped. The adherends have a thickness of 3 mm and length of 100 mm, and the width of the sample is 25 mm. The FBG sensors were inscribed using UV femtosecond laser and phase mask technique, with a similar laser configuration as described in [48]. The UV output power was fixed to 200 mW and focused to the core of the optical fiber with a cylindrical lens of 50 mm focal length. Short length (6-8 mm) FBGs were inscribed to ensure uniform stress distribution along the sensor when embedded centrally in the adhesive layer. We verified this

with 3D FEM modeling using commercially available Abaqus FEA software [49]. The modeling approach is explained later in this section. The butterfly MOF-FBG sensors feature a 2.4 mol% GeO₂-doped inclusion, as indicated in Fig. 1. As discussed earlier in section 2, the optomechanical response of butterfly MOF-FBG sensors features an angular dependence. After testing the samples, the cross-sectional sides of the adhesive layer are polished to verify the optical fiber position and orientation (Table 1). The results show that it is perfectly possible to position an optical fiber and maintain its angular orientation within $\pm 9^\circ$ in a SLJ without the need to adapt the SLJ fabrication procedure. Previous research [47] demonstrated that for the butterfly MOF sensor an angular misalignment of 10° from its optimal transverse strain sensing direction, leads to a sensitivity decrease of 10%. To facilitate fiber orientation in larger structures, one can consider the use of alignment tabs fixed on the optical fiber that indicate the optimal orientation. Another option is to adapt the outer cladding of the butterfly MOF to feature a flat side, also known as a D-cladding shaped fiber. The alignment tabs or the flattened side of the fiber can help to maintain the optimal fiber orientation during fiber positioning in the host material. Chehura *et al.* [50] demonstrated that the transverse strain sensitivity of the modal birefringence of an elliptical core fiber is not significantly affected when the circular outer cladding is changed to a D-cladding shape.

Table 1. Overview of the experimental and 2D FEM results for SMF-FBG and butterfly MOF-FBG sensors embedded in SLJs. For SMF-FBG sensors, the sensor response to a tensile load corresponds to the shift of the individual Bragg peak wavelength. In case of the butterfly MOF-FBG sensors, this response corresponds to the shift of the Bragg peak wavelength separation.

	<i>Single mode fiber</i>			<i>Butterfly MOF</i>		
	<i>Exp, 1A</i>	<i>Exp, 1B</i>	<i>FEM, 3D</i>	<i>Exp, 2A</i>	<i>Exp, 2B</i>	<i>FEM, 2D</i>
Overlap length (mm)	27.88	28.05	28.0	25.80	26.55	25.0
Bond thickness (mm)	0.68	1.02	1.0	0.83	1.39	0.8
Fiber orientation ($^\circ$)	-	-	-	-39.9	-53.5	-45
Fiber location x (mm)	-0.32	-0.66	0	-0.02	-0.42	0
Response peak 1 (pm/kN)	-	-	-	-130.5	-137.6	-
Response peak 2 (pm/kN)	-	-	-	-63.1	-65.8	-
Sensor response (pm/kN)	-38.3	-42.0	-39.3	67.4	71.8	69.9

The reflection spectra of the FBG sensors are recorded before and after embedding in a SLJ (Fig. 3(a) and Fig. 4(a)). Minor spectral deformations were introduced, but this did not affect the Bragg peak detection. An average shift of 669 ± 9 pm of the Bragg peak wavelengths towards longer wavelengths was detected for all samples. This shift is likely due to axial strain induced during SLJ fabrication when fixing the fiber to maintain its position and angular orientation in the adhesive layer.

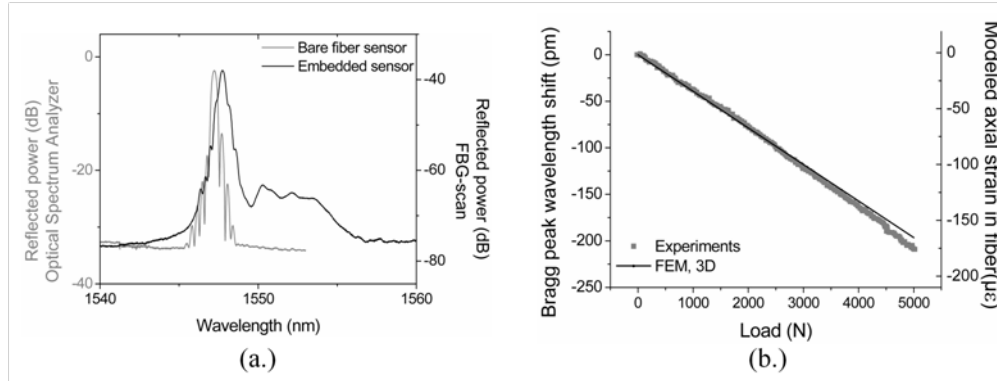


Fig. 3. Sample 1B: (a) SMF-FBG reflection spectra before and after embedding the sensor in the SLJ show minor deformations and a shift toward longer wavelengths due to axial pre-strain. (b) Results from experiments and 3D FEM modeling demonstrate a transverse contraction due to tensile loading of the adhesive layer which transfers a negative axial strain on the fiber. Since the axial strain sensitivity of SMF-FBG sensors is known to be $1.2 \text{ pm}/\mu\epsilon$, we find a good match between 3D FEM results and experiments.

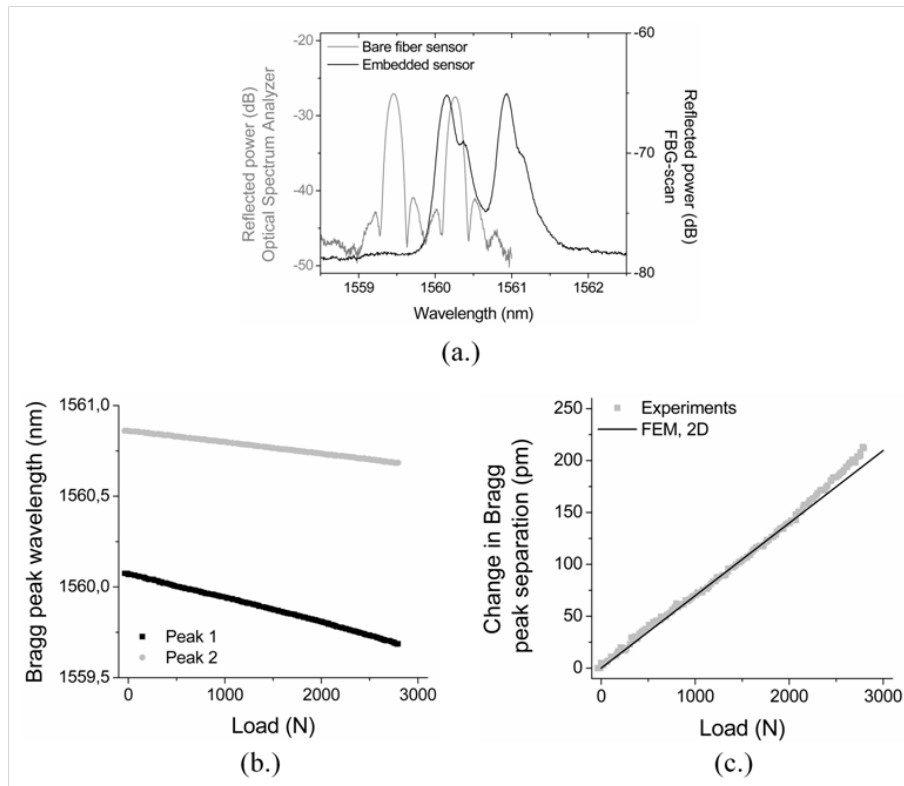


Fig. 4. Sample 2A: (a) Butterfly MOF-FBG sensor reflection spectra before and after embedding the sensor in the SLJ show minor deformations and a shift toward longer wavelengths due to axial prestrain. (b) The individual Bragg peaks shift towards lower wavelengths due to tensile loading of the SLJ. From linear fitting the results up to a load of 2 kN, we find that their sensor response is respectively $-136.0 \text{ pm}/\text{kN}$ and $-63.5 \text{ pm}/\text{kN}$ for the Bragg peak 1 and Bragg peak 2. (c) The Bragg peak separation increases due to tensile loading with a sensor response of $67.4 \text{ pm}/\text{kN}$. Results from 2D FEM modeling of a SLJ similar to sample 2A are in very good agreement with the experimental results.

The sample is placed in a hydraulic servo-controlled tensile test machine with a load capacity of 100 kN (Instron 8801 [51],) by gripping it at both ends (Fig. 5). A static tensile load is applied at a rate of 0.05 mm/min until failure of the SLJ. During loading, the FBG sensor response is recorded using an FBG interrogator (FBG scan 608 [52],) with a sample frequency of 1 Hz and peak detection resolution of 1 pm.

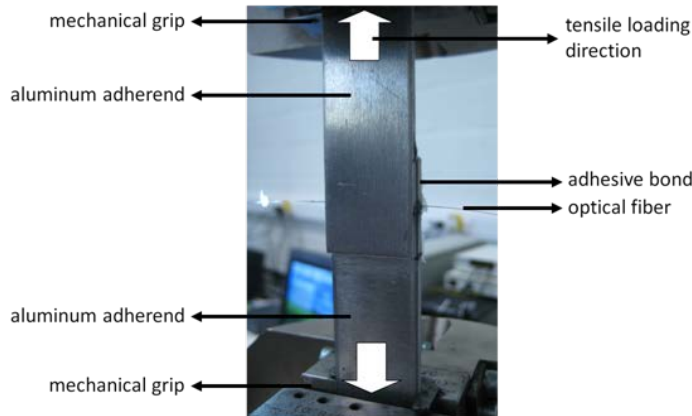


Fig. 5. Picture of the SLJ sample placed in the tensile test machine. The optical fiber is also visible.

The SMF-FBG sensor response to tensile load of sample 1B is shown in Fig. 3(b). The results of a linear regression analysis of the response of samples 1A and 1B yielding the sensitivity in pm/kN are given in Table 1. For both samples the Bragg peak wavelength shifts to shorter wavelengths because of tensile loading of the SLJ. This corresponds to an axial compression of the FBG sensor that is induced by transverse contraction of the adhesive layer. This was verified with a 3D FEM model with dimensions corresponding to that of sample 1B and a silica rod located centrally in the adhesive layer to represent an optical fiber. Constraints are applied to the adherends to reproduce a fixed support on the left and a guided support on the right end of the SLJ. A load of maximum 5 kN is applied to the right end. The mesh consists of linear, 3D stress elements. Perfect bonding is assumed at all interfaces. The elastic modulus E and Poisson coefficient ν is respectively 70.0 GPa and 0.33 for the aluminum adherends, 0.47 GPa and 0.385 for the MMA adhesive, and 72.5 GPa and 0.17 for the silica optical fiber. The actual material parameters for the two component MMA structural adhesive were not available. Therefore, an average was made over publicly available material parameters (E and ν) available for similar two-component MMA adhesives [53–55]. Results from 3D structural FEM modeling show that the detected negative Bragg peak shift is indeed because of transverse contraction of the adhesive layer, and results in a (negative) axial strain that is transferred to the optical fiber. Figure 3(b) compares the results of the experiment with those of 3D FEM when using the well-known axial strain sensitivity of SMF-FBG sensors (1.2 pm/ $\mu\epsilon$ [3,39],) to calculate the corresponding Bragg peak shift. We find a very good agreement between experiments and 3D FEM modeling of SMF-FBG sensors embedded in a SLJ.

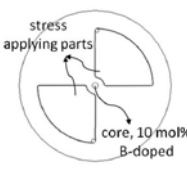
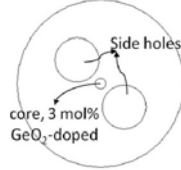
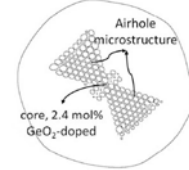
The butterfly MOF-FBG sensor response of sample 2A is shown in Fig. 4 and the results of a linear regression analysis of that response against applied load is also given in Table 1. For sample 2A, the Bragg peak separation increases because of tensile loading of the SLJ at a rate of 67.4 pm/kN. We limited the linear fit up to 2 kN, since at higher loads the sensor response is no longer linear. This can be attributed to the initiation and growth of cracks at the edge of the adhesive bond. Debonding at the edges will increase the shear stress at the location of the optical fiber. The experimental results were verified using 2D structural FEM modeling of a SLJ model using the same constraints, loading conditions and material

properties as mentioned before. The dimensions of the adhesive layer and SLJ were chosen to match that of sample 2A. The 2D model of the butterfly MOF was extracted from its scanning electron micrograph (SEM) as shown in Fig. 1 [47]. We have limited the simulations to 2D FEM since the sensing principle of the butterfly MOF-FBG sensor relies on the change of material birefringence which is limited to effects in the xy -plane. Moreover, we obtained a very good agreement between experiments on a SMF-FBG sensor and 3D modeling, which gives us confidence that neglecting stress along the z -direction will not affect the results for the Bragg peak separation. The result from a 2D FEM model of the peak separation is shown in Fig. 4(c) and summarized in Table 1. A sensor response of 69.9 pm/kN is obtained, which agrees well with the experimentally obtained value. For sample 2B, the Bragg peak separation increases at a rate of 71.8 pm/kN. The slightly higher response stems from the thicker bond and from the small off-centre location of the fiber. Both of these effects increase the shear stress at the location of the fiber.

The increase in peak separation is due to the angular orientation of the MOF sensor, -45° instead of $+45^\circ$, and prevents peak overlapping and corresponding peak detection errors. Since both peel and shear stress are present in the adhesive layer, we cannot link the rate of change entirely to shear stress alone. However, because of the particular orientation of the MOF sensor, we can say that its sensitivity to the small amount of peel stress will be minimal. The shear and peel stress profiles shown in Fig. 2(b), which are derived from this particular 2D FEM model, show that in the centre of the adhesive layer the shear stress is 1.18 MPa when a tensile load of 1 kN is applied to the SLJ. On the other hand, the peel stress at that location is more than 3 times smaller: only -0.35 MPa. In the experiment on sample 2A, a load of 1 kN induced a peak separation increase of 70.6 pm. Hence, when neglecting peel stress, the butterfly MOF-FBG sensor would have a shear stress sensitivity of 59.8 pm/MPa. Considering the material properties of the adhesive, this sensitivity would correspond to a shear strain sensitivity of 0.01 pm/ $\mu\epsilon$. It should be noted that although shear stress in an optical fiber is known to induce optical mode coupling between the fundamental modes [56], the modal birefringence of the butterfly MOF is sufficiently large to prevent the occurrence of this effect. During our experiments, we did not experience any detectable change in the reflected optical power of both fundamental modes.

To demonstrate the added value of the butterfly MOF-FBG sensor over other types of highly birefringent fiber with an outer cladding diameter of 125 μm and a doped inclusion in the core region, we have also modeled the sensitivity of a bow-tie and side-hole fiber when embedded in a similar SLJ. We have constructed 2D FEM models of these fibers based on details and dimensions provided by Guan *et al.* [58] and by Clowes *et al.* [59]. An overview of the results is presented in Table 2. When embedded in a SLJ, the bow tie FBG sensor and side hole FBG sensor yield a shear stress sensitivity of 16.0 pm/MPa and 16.2 pm/MPa, respectively. These shear stress sensitivities are almost 4 times lower than that obtained with a butterfly MOF-FBG sensor, clearly indicating the added value of our dedicated MOF-FBG sensor.

Table 2. Results of a 2D FEM comparative study of the shear stress sensitivity of different highly birefringent FBG sensors. For completeness, we also present an overview of earlier reported (experimental) sensitivities for the sensitivity to temperature and hydrostatic pressure of these fibers and their transverse strain sensitivity when embedded in a laminated composite material. Sensitivities indicated with * are derived from the polarimetric sensitivity.

	Bow tie fiber	Side hole fiber	Butterfly MOF
Bare fiber – Thermal sensitivity	–0.7 – + 0.22 pm/°C [57,58]	–0.04 pm/°C [9]	–0.07 pm/°C [47]
Bare fiber – Hydr. pressure sens.	+ 0.65* pm/MPa [34]	+ 7.6 – + 9.2* pm/MPa [9,59]	–15 – + 33 pm/MPa [35]
Embedded – Transverse strain sens.	–0.022 pm/με [41]		–0.16 – + 0.29 pm/με [39,47]
2D FEM model			
Model properties	[58]	[59]	[34]
Bare fiber – Hydr. pressure sens.	+ 0.8 pm/MPa	+ 6.7 pm/MPa	–17.4 pm/MPa
Embedded in a SLJ – Shear stress sens.	+ 16.0 pm/MPa	+ 16.2 pm/MPa	+ 59.8 pm/MPa

4. Conclusion

We have successfully demonstrated, for the first time to our knowledge, shear stress sensing with Bragg grating-based sensors fabricated in a highly birefringent butterfly MOF. The functionality of our shear stress sensor was validated by integrating the sensor in the adhesive of a single lap joint. When this joint was loaded in tension, we obtained a shear stress sensitivity of 59.8 pm/MPa. This corresponds to a shear strain sensitivity of 0.01 pm/με. We have verified our experimental results with 2D and 3D FEM modeling. Compared to conventional birefringent fibers, our dedicated MOF design yields a fourfold sensitivity improvement. This clearly demonstrates the added value of MOF-FBG sensor technology. Moreover, since the butterfly MOF-FBG sensing principle relies on the change in modal birefringence when subjected to shear loading, our technology carries significant potential for temperature insensitive shear stress sensing.

Acknowledgments

The authors would like to acknowledge financial support from the Agency for Innovation by Science and Technology (IWT Grant 101221 and IWT contract 120024), the European Commission's Seventh Framework Programme projects 'SMARTSOCKET' (FP7-PEOPLE-IAPP-2009 Grant Agreement 251649), the COST TD1001 action 'OFSeSA', the Research Foundation–Flanders (FWO-Vlaanderen), the Methusalem and Hercules Foundations

Flanders. The authors also wish to thank the SURF research group at Vrije Universiteit Brussel for their assistance with the fiber cross-section SEM pictures.